Quantifying natural delta variability using a multiple-point geostatistics prior uncertainty model

Céline Scheidt[1], Anjali M. Fernandes[2], Chris Paola[3], and Jef Caers[4]

[1]Energy Resources Engineering, Stanford University, USA

[2]The Center for Integrative Geosciences, University of Connecticut, USA

[3]Department of Earth Sciences, University of Minnesota, USA

[4]Department of Geological Sciences, Stanford University, USA

Corresponding author: Jef Caers (jcaers@stanford.edu)

Key Points:

* Quantifying uncertainty associated with autogenic variability

* Reproducing natural variability using multiple-point geostatistics with a limited set of training images

* Representing autogenic pattern variability with a small set of physically meaningful 'eigen patterns'

This article has been accepted for publication and undergone full peer review but has not been through the copyediting, typesetting, pagination and proofreading process which may lead to differences between this version and the Version of Record. Please cite this article as doi: 10.1002/2016JF003922

Abstract

We address the question of quantifying uncertainty associated with autogenic pattern variability in a channelized transport system by means of a modern geostatistical method. This question has considerable relevance for practical subsurface applications as well, particularly those related to uncertainty quantification relying on Bayesian approaches. Specifically, we show how the autogenic variability in a laboratory experiment can be represented and reproduced by a multiple-point geostatistical prior uncertainty model. The latter geostatistical method requires selection of a limited set of training images from which a possibly infinite set of geostatistical model realizations, mimicking the training image patterns, can be generated. To that end, we investigate two methods to determine how many training images and what training should be provided to reproduce natural autogenic variability. The first method relies on distance-based clustering of overhead snapshots of the experiment; the second method relies on a rate of change quantification by means of a computer vision algorithm termed the demon algorithm. We show quantitatively that, with either training image selection method, we can statistically reproduce the natural variability of the delta formed in the experiment. In addition, we study the nature of the patterns represented in the set of training images as a representation of the 'eigen-patterns' of the natural system. The eigen-pattern in the training image sets display patterns consistent with previous physical interpretations of the fundamental modes of this type of delta system: a highly channelized, incisional mode; a poorly channelized, depositional mode; and an intermediate mode between the two.

1 Introduction

A fascinating connection exists between uncertainty in predicting future states of geomorphic systems and predicting the subsurface structure of their depositional products: both forms of uncertainty are fundamentally associated with our lack of detailed knowledge about possible spatial configurations of the system. Channelized transport systems – fans, rivers, deltas, and their submarine analogs – reconfigure themselves more or less continually in time, through various forms of channel instability including meandering, bar growth and decay, and channel avulsion. Changes in configuration in channelized systems can be triggered by external causes, but much of the change is the result of the internal dynamics of the system itself, i.e. it is autogenic [*Kim et al*. 2014]. It is not known if the autogenic behavior of natural channels is, in a strict sense, chaotic [*Lanzoni and Seminara* 2006], but at present it is clear that one cannot predict with certainty the detailed configuration of even a single meandering channel very far into the future, let alone a channel network. This lack of predictive ability is mirrored in a parallel inability to predict with certainty the configuration of channel deposits in the subsurface away from control points such as wells. We stress here that uncertainty is inherent in the dynamics of the system, and is not due, for example, to observational error (extensive discussion on forms of uncertainty can be found in *Caers* [2011]).

In this paper, we propose a new approach to quantifying uncertainty associated with autogenic pattern variability in a channelized transport system, with possible applications to both surface and subsurface forecasting. Specifically, we focus on a powerful and relatively new form of geostatistical pattern simulation, termed multiple-point geostatistics (MPS; *Strebelle* [2002]; *Caers & Zhang* [2004]; *Mariethoz & Caers* [2015]), in which the possible configurations of a target system are represented by a limited set of training images. MPS then aims to simulate alternative states of the system by, in a sense, statistically re-arranging

the training image patterns in a manner that preserves their essential structure while generating an unlimited number of possible realizations of that structure. This not only has enormous practical application in terms of analyzing risk and uncertainty owing to our inability to forecast these patterns, but also opens a series of tantalizing questions about what the 'essential nature' of a pattern might mean mechanistically. In this work we focus on some initial questions raised by this line of thought: the number of training images required to capture the essence of a physically generated pattern; the extent to which these training images function as a set of 'eigenpatterns' that represent the essential configurations the system can take on; and, assuming such a set of training images exists, the best way of finding it from a large set of observed system configurations. To set the stage for our study, we turn next to a more detailed look at uncertainty, focusing on the subsurface case.

Quantifying uncertainty on predictions made in subsurface sedimentary systems has considerable practical relevance for applications such as energy production, storage, groundwater management, salt water intrusion and contaminant remediation, to name a few. Such uncertainty is due to a lack of understanding of the subsurface, which is due to the fact that one cannot exhaustively sample the subsurface system in detail. The quest for uncertainty quantification is therefore a quest for quantifying our lack of understanding. While many methods and techniques have been and are still being developed, at a deep level, we do not fully understand the very nature of uncertainty and variability in natural systems such as sedimentary systems.

If quantifying uncertainty is about lack of knowledge or information, then such quantification calls for a theory of information. Many such theories exist [*Bayes & Price*, 1763; *Dempster*, 1967; *Shafer*, 1976; *Zadeh*, 1978] but in this work we will be considering the question of uncertainty within the realm of Bayesian information theory [*Jaynes*, 2003]. If we term the entire system (e.g. a subsurface system), with all of its details and properties, "the system", and we term any information we obtain on this system through measurements (e.g. wells, geophysical measurements), "information", then Bayes' rule states simply that

$$\mathrm{P}(\text{system}\,|\,\text{information}) = \frac{\mathrm{P}(\text{information}|\text{system})}{\mathrm{P}(\text{information})} \times \mathrm{P}(\text{system}) \quad (1)$$

Because the left-hand side is a probability (or probability density) and needs to sum (or integrate) to unity, Eq (1) is also written in proportional form as

$$\mathrm{P}(\text{system}\,|\,\text{information}) \propto \mathrm{P}(\text{information}|\text{system}) \times \mathrm{P}(\text{system}) \quad (2)$$

Bayes' rule states therefore that the reduced uncertainty of a system (as modeled by a conditional probability of the form P(A|B) informed by some information depends on some initial uncertainty (initial understanding or lack of knowledge) about the system, multiplied by a factor that involves how likely the information is for any given system state (the likelihood). In Bayesian thinking, information can only reduce uncertainty, it cannot increase uncertainty, relative to what is known initially (meaning before obtaining any information). The resulting probability is termed the posterior distribution. Clearly any quantification of uncertainty will depend on these two terms and in the presence of limited information, the prior term has considerable impact on the ultimate posterior uncertainty quantification.

Our MPS analysis in this paper can thus be thought of as a way of better understanding and quantifying "prior uncertainty". Approaches in statistical science usually aim for parameterization of the system and statement of probability distributions on such parameterization motivated through general principles or concepts [*Jaynes*, 2003]. One such general principle is the principle of maximum entropy [*Shannon*, 1949; *Jaynes*, 2003], often leading to uniform, exponential or Gaussian distributions when choosing specific statistical constraints [*Cover & Thomas*, 2012]. However such approaches neglect physical constraints in sedimentary systems and thus understanding of the processes that create a specific stratigraphy, beyond these general principles. A quest for quantifying prior uncertainty therefore necessitates understanding the sedimentary system by means of physical principles. Consider the example of deltas, an especially important type of channelized system [*Vorosmarty et al*., 2007]. Quantifying prior uncertainty would require stating all configurations of deltas deemed physically possible and a probability density associated with each configuration. This probability density need not be Gaussian or uniform. Hence, the question arises: what is this probability density for possible delta configurations, and how does one represent it in a form that can be used for actual predictions using Bayes' rule?

As we stated above, the observation that deltas can take on a range of forms arises mostly from their intrinsic ("autogenic") variability. Suppose one could create a large number of deltas using the same initial boundary conditions (i.e. sediment and water supply, grain size distribution, etc.). Even if created under effectively identical conditions, each delta would nonetheless each take on a somewhat different form. Our overall goal is to develop methods to quantify natural pattern variability, with application to constraining uncertainty in subsurface reconstructions, as well as in Earth-surface forecasting ("Earthcasting").

The data for our study of quantification of natural delta variability comes from laboratory experiments. In the laboratory, an experiment can be run under constant forcing for long enough to provide many different realizations of the autogenic variability – a situation that would be practically impossible to find in the field. The autogenic variability in these systems is due to temporal and spatial variability in the feedback between flow and sediment transport, weaving the internal fabric of the final subsurface system. We use data from an experiment, subject to fixed and known boundary conditions (e.g.: water and sediment flux, base-level changes), where variability in flow patterns and deposition is known and quantifiable if a measure of variability can be defined. In this paper, we tackle therefore the specific and more limited question of whether geostatistical methods can capture the natural variability of the autogenic cycles. In MPS, the method we use here, prior uncertainty is formulated based on a limited set of training images, which we propose can be chosen so as to represent the basic 'eigenpatterns' of the system. The structure of our work is therefore as follows. We first introduce the laboratory experiment on which our analysis will be based. Since our work is aimed at both the geostatistical and Earth-surface dynamics communities, we introduce scientific components needed to make our work comprehensible to readers from both fields. In the next section, we describe the experiments, and then review data-scientific methods in the following section. The rest of the paper focuses on selection of training images as used for MPS, and formulating the prior uncertainty model with MPS. We then analyze the uncertainty model and compare them with the natural variability generated in the laboratory experiments.

2 The Experimental Delta Data-set

The central data set for our analysis is a set of overhead images of a delta constructed in an experimental sedimentary basin subject to constant external boundary conditions (i.e. sediment flux, water discharge, subsidence rates). Basin dimensions were 4.2 m long, 2.8 m wide and 0.65 m deep. Water discharge was held constant at 0.451 L/sec, sediment discharge constant at 0.011 L/sec and the ratio of water discharge to sediment discharge was 40:1. The sediment consisted of a mix of 70% quartz sand (D50 = 110μm) and 30% anthracite coal sand (D50 = 440 μm). The data set used is a subset of the data collected during an experiment in the Tulane Delta Basin, conducted in 2010 [*Wang et al*., 2011].

In this experiment, the mean shoreline position was held constant by balancing the sediment discharge against the steady base-level rise rate of 5 mm/hr. Under fixed boundary conditions, the observed variability in deposition is therefore the result of only the autogenic (intrinsic) variability in the transport system. The geostatistical analysis we report here is based on a set of 136 time-lapse overhead photographs that capture the dynamics of flow over the delta approximately every minute. Figure 1a shows representative images from this database. This set of images represents a little more than two hours of experimental run time. Figure 1b shows the binary (wet-dry) images for the same set and Figure 1c shows the set when discretized into four categories. The sets illustrated in Figure1 b and c are used for statistical and physical analysis of the images in later sections of the paper.

3 Data scientific tools

3.1 Modeling prior uncertainty with MPS

In this paper, we model prior uncertainty in Eq. (1) and (2) using multiple-point geostatistics (MPS). In MPS, spatial or spatio-temporal variability is quantified using an example, termed the training image (TI) [*Mariethoz & Caers*, 2015] (see Figure 2), although the word "image" should not be regarded as limited to 2D. The training image represents the fundamental patterns, and the idea of MPS is to replicate patterns in the training image to create many stochastic realizations, possibly including some trend. If only one TI is proposed, then the possibly infinite set of realizations constitutes a sampled version of that prior uncertainty. In the same sense, samples of a Gaussian distribution represent the statistical variation of the Gaussian distribution. Any finite sample represents an approximation of the stated distribution. Unlike the Gaussian distribution, in MPS, no explicit mathematical expression of the prior uncertainty model is provided. Here lies also one of the major differences between MPS and probability-based method such as Markov Random Fields (*Kinderman et al*., 1980). MPS algorithms often rely more in principles of computer science rather than purely mathematical ones. The reason lies in the lack of simple mathematical models to represent the higher-order statistics present in complex pattern variation. Methods such as MRF that have explicit mathematical models become intractable for large problems with complex pattern variations (*Mariethoz & Caers*, [2015]).

It is unlikely that all possible naturally occurring patterns can be contained in one single training image. As a result, the current trend in geostatistics is to express uncertainty on the TI by proposing many TIs [*Park et al.*, 2013; *Scheidt et al.*, 2015; *Demyanov et al*., 2015, *Linde et al*., 2015]. From each TI, one can generate many realizations, and the total set of all these realizations then constitutes a much wider prior uncertainty model. Figure 2 illustrates this idea, showing an example of three alternative training images (left) as well as a few geostatistical realizations for each one (right). Research in MPS has now arrived at the following question: how many training images should one use and how does one select these training images? Ideally, the TIs should be generated in such a way that natural variability of the system under study is represented (fluvial, deltaic, turbidite, etc.), hence that all possibilities are covered in the possibly infinite set of geostatistical realizations. Under these conditions, one can view the TI set as representing the fundamental 'eigenpatterns' of the system, and the geostatistical realizations as representing, in effect, an infinite set of potential stochastic rearrangements of the members of that eigenpattern set. Eigenpatterns should be understood in the broad sense and do not necessarily represent an orthogonal decomposition in the strict mathematical sense.

3.2 Variability in a set of images as expressed by distances

Comparing variability between two sets of images is a requirement for this work and hence requires detailing. Traditionally, variability is expressed by means of variance or covariances, but such measures may fall short in capturing variation in complex phenomena [*Gomez-Hernandez & Wen*, 1998; *Strebelle*, 2002; *Feyen & Caers*, 2006; *Tan et al.*, 2014]. Another more suitable approach is to extract certain statistics from each image and compare those statistics (e.g. *Liang et al*. [2016]).

In this work we rely on the formulation of distances between any two images to capture such variability. Consider any two images. The question then is how to define a meaningful difference between any two images. Taking the average square difference between the pixels in each image may be simple, but does not lead to a good discrimination between the various images, see for example Figure 3. Hence the choice of the distance is important and should be chosen such that it capture difference in what are considered salient features in the image.

Based on experience gained in previous work, with similar settings [*Suzuki & Caers*, 2008; *Suzuki et al*., 2008], we use the Modified Hausdorff Distance (MHD, *Dubuisson & Jain* [1994]), which is a static/geometric measure evaluating the distance between spatial objects. An image, such as a binary overhead snapshot (Figure 1b) contains such objects and hence we would like to quantify how this differs from the objects in any other overhead snapshots. The MHD does not directly work with the objects but with the edges of the objects, hence the images are converted first to edges, which are then represented as point-sets (the collection of pixels representing the edge), see Figure 3. The problem now is to define a distance between point sets. To that end we first define a distance *d(a,B)* of a point *a* to point set *B* as the distance of *a* to the closest point of *B* (Eq. 3). Then the distance *d(A,B)* between point sets *A* and *B* is the average of those distances (Eq. 4). Note the *d(A,B)* is different from *d(B,A)*, which would violate one of the axioms of a distance (symmetry). To alleviate this problem one simply uses the maximum (Eq. 5), which restored the symmetry ($\max(x,y)=\max(y,x)$).

$$d(a,B) = \min_{b\in B} \|a-b\| \quad (3)$$

$$d(A,B) = \frac{1}{N_a}\sum_{a\in A} d(a,B) \qquad d(B,A) = \frac{1}{N_b}\sum_{b\in B} d(b,A) \qquad (4)$$

$$MHD = \max\left(d(A,B), d(B,A)\right) \quad (5)$$

MHD allows for a better distinction of different shapes than a simple pixel by pixel difference, as illustrated in Figure 3. Visually, the images of numbers 1 and 7 are more similar than the other combinations, which is what the MHD measure finds. However, the Euclidean, pixel-by-pixel difference shows a different result.

The next question is how to provide a visualization of these differences or how to compare differences. For example we may have three sets of images (set1, set2 and set 3) and would like to compare, visually, the difference between each sets of images: is set1 more different from set2 than set3 or are they equally different? One simple way to visualize this is to make QQ-plots (quantile-quantile plot), i.e. to make a comparison of the empirical distributions of distances between set1 and set2 with the distances between images in set1 and set3.

However, one can go even further than this simple univariate comparison. Images can be seen as objects in a high-dimensional space. For example an image with M pixels can be represented in an M dimensional Cartesian axis system, each pixel represented by an axis. Each image is then simply a point in that space. How do we visualize these point distributions (the cloud of points) in a meaningful way? For one, we care only about the distances between images, not where exactly this point lies in the Cartesian space. In other words, we are interested only in relative distances, not absolute coordinates. Multi-dimensional scaling (MDS, *Borg & Groenen,* [1997]) is a projection method that allows projecting objects in high-dimensional space to a low-dimensional space, for example 2D, 3D, attempting to preserve the distances between these objects (in a least-square sense) as much as possible. In summary, MDS takes an NxN distance table and creates a 2D (or 3D) plot, such that the Euclidean distances in the projection approximate, in least-square sense, the distances in that table. The resulting scatterplot of points, where each point refers to an object, is used as a visual appraisal of the distribution of higher dimensional objects. Figure 4 presents a 2D visualization of the wet/dry images in MDS space. The MHD was used in this case to obtain a 136 by 136 distance table (the set of snapshots contains 136 images) for MDS.

3.3 Quantifying change between images: the demon algorithm

Commonly, a depositional system alternates between abrupt changes in the deposition (major re-organization) and small, gradual changes. Hence, another way to look at variability is to quantify the change from one snapshot to the next one; this has the added appeal that pattern change is also critical in how surface patterns are recorded as stratigraphy. We propose to study local changes in time in the snapshots using the demon algorithm [*Thirion,* 1996; *Li et al*., 2015]. The demon algorithm is a gradient-based algorithm that determines "forces" that are required to deform a given image into a target image (Figure 5). The demon algorithm calculates for each pixel, changes in the x and y directions that must be applied to the image being changed (left on Figure 5) to produce an image as close as possible to the target image (right on Figure 5). Resulting from the demon algorithm are two maps Tx and Ty, of the same size as the original images, representing the x and y components of change respectively.

Hence, each pixel in this map represents how much translation (in the x-direction and y-direction respectively) the starting image underwent at that location to match the target image. In Figure 5, one observes how such translation is small in areas where the images match (both black) and high in areas with a mismatch. Since (Tx,Ty) represents a vector, a L2-norm (the length of that vector) can be used to summarize the total amount of change (irrespective of orientation), see Figure 5. A large norm indicates a large change at that location. Because the demon algorithm attempts to transform one image into a different image using gradients, only images relatively close to each other are suitable for this method. Hence, the demon algorithm is only applied to images consecutive in time (as opposed to the MHD previously, which was applied between any pair of images in the set). Figure 6 illustrates this concept but the demon algorithm is now applied to five images from the experiment. Note that here the images discretized images shown in Figure 1c are used, for better convergence. Small difference exists between time 4 and 5 but large difference between 7 and 8 (bottom, right corner), resulting in a large norm.

3.4 Selecting a representative subset of images from a larger set

In this section we address the question of how many images and which images are needed to represent the entire set with reasonable accuracy. In univariate statistics we know that quantiles can be used as representations of a univariate distribution: the more quantiles, the more accurate the distribution is represented. If a distribution is complex (e.g. multi-modal or skew) then more quantiles are needed. The concept of quantiles does not easily extend to higher dimensions because there is no unique or natural ordering in higher dimensions (e.g. *Serfling* [2002]), hence other methods must be used. Here, we present two very different ways of selecting representative images from a given set: one based on purely statistical principles and one based on physical intuition.

3.4.1 Distance-based clustering

The statistical approach to selection is based on the definition of a distance between images. Namely, images that are close to each other could be represented by one single image. It would not make sense to select two training images that are very similar. To visually illustrate this, Figure 4, shows an MDS plot of the 136 overhead snapshots, with the modified Hausdorff distance. Each point in that plot represents an image and clearly images are clustered; they are not uniformly distributed. In Figure 4, this is a 2D space, but in all rigor, a distance defines a metric space, namely a space without any axis system. Clustering algorithms allow for selecting representative images, based on a definition of distance (e.g. *Scheidt and Caers* [2009a,b]). The particular algorithm used here is the k-medoid algorithm. This iterative algorithm requires the user to specify the amount of images to select, *N*. In essence, the method selects the set of *N* images by iteratively partitioning the space (e.g. in the MDS plot) in regions of similar images. Unlike the k-means algorithms, which returns average images (averaged over the group), k-medoid returns the "middle" image of a group.

Discovering the number of clusters (*N*) innate to a set of objects is the topic of unsupervised clustering and requires further definition. Clearly a compromise has to be found between putting all images in one group and making a group for each single image. Measures that are used in achieving this, seek a balance between within-cluster variability and between-cluster variability. In this paper, we will use the silhouette index as the appropriate measure [*Rousseeuw*, 1987]; this index has been found to be quite robust with respect to the selection

of *N*. The silhouette index measures the quality of the clustering configuration by measuring how compact the clusters are. A good configuration consists of compact clusters, which are clearly separated from other clusters, resulting in a high silhouette index (close to 1).

3.4.2 Selection by means of the demon algorithm

Although time is clearly correlated in the MDS plot of Figure 4, the above procedure for selection does not make explicit use of the fact that the images are in a sequence. Therefore, an alternative approach to selection is to analyze periods of time when the system changes versus periods of time when it stays relatively stable. This requires a quantification in the rate of change in the system. If the changes between consecutive images are similar in terms of location and intensity, only a few images can be selected to represent the variability of the system. On the other hand, if the changes between consecutive images are significant, more images may be necessary to represent flow patterns in that time period.

4 Analysis of the selected images

4.1 Selecting representative images

We now turn to discussing the main results starting by selecting images that best represent the 136 images of the experimental delta. These images will then later be used as training images in creating a geostatistical prior uncertainty model. In Figure 7 are shown the selected training images using clustering based on the MHD; the basic idea is to select images in the center of each cluster, as viewed in the distance-metric space. The silhouette index method resulted in a selection of 5 images. Figure 8 shows the clustering results in an MDS plot. The points are colored by clusters, the squares indicating the medoids of each cluster (i.e. the selected images).

An alternative selection was made based on the local rate of change in the system calculated with the demon algorithm. To capture such local change, four regions are created, based upon their proximity to the source of sediments (see Figure 9). This geometry can be indicative of how much downstream change was propagated from upstream versus how much is local. The rate of change is defined as:

$$r_t = \frac{1}{4}\sum_{k=1}^{4}(\bar{n}_t^k - \bar{n}_{t+1}^k)$$

using differences in the maps of norms $\bar{n}_t^k$(intensity in change) over region *k* (shown in Figure 9) provided by the demon algorithm.

Figure 10 shows the rate of change r_t of the system as a function of time for the experiment. The peaks represent a large rate of change, whereas valleys represent a low rate of change. We observe that the changes of the system do not occur at a regular rate; rather, some periods of time have low changes (times t = 10 min to t = 35 min) and other similar lengths of time have significant changes (times t = 55-70 min, t = 75-82 min). Representative images are then selected from periods between peaks (significant reorganization of the system); in this case one can view the representative images as characteristic of relatively stable states of the system. The peaks used for the selection are indicated with a red line in Figure 10. We chose

five of the highest peaks, which were spaced well apart, by eye. Between the peaks, we chose images at times when the changes of the system are small and similar in nature (i.e. one image within each interval, with low rate of change and relatively centered), indicating relative stability of the system. The six selected images are displayed in Figure 11; they look significantly different and represent different patterns.

4.2 Eigen patterns represented by the selected images

We now investigate more closely the characteristics of the two sets of selected images in terms of the following physical properties (see Figure 12):

1. The ratio of total number of wet pixels (black in Figure 1b) to the total number of dry pixels (white in Figure 1b) in the binary images, which provides us with a metric for the wetted area at any one point in time. Approaches using the total wet pixels or dry pixels have been used in a number of experimental fluvial studies in the past (eg: *Wickert et al*. [2013])

2. The ratio of deep to shallow flow in the categorized images, which is calculated by summing the pixels with the most intense blue dye (the black pixels in Figure 1c) and those with the paler shades of blue (intermediate and pale grey pixels in Figure 1c).

These metrics define a continuum between channelized flow and sheet flow (Figure 13), which have been shown to be associated with periods of sediment flushing and storage respectively [*Sheets et al*., 2002]. Periods of sediment removal or downstream flushing are characterized by laterally restricted, deep flow within a few dominant channels. Such patterns are tied to shoreline progradation and a reduction of channel gradient in the downstream direction [*Kim et al*., 2006]. Reducing the channel gradient leads to a decreased sediment transport capacity and in-channel deposition. Conversely, channel-filling results in flow expansion, inundation of the experimental surface by sheet flow, wide-spread deposition, and shoreline retraction.

High ratios of wet to dry pixels combined with low ratios of deep to shallow flow are indicative of patterns dominated by sheet flow, when greater deposition occurs. Low ratios of wet to dry pixels and high ratios of deep to shallow flow represent a greater degree of channelization on the experimental surface, and are characteristic of periods of sediment erosion. We note that the original dataset and training images from both protocols (MHD and demon), encompass the range of surface configurations that include: 1) Pattern 1: Channelized flow, 2) Pattern 2: Sheet flow, and 3) Pattern 3: Intermediate between the two extremes.

4.3 Reworking of the experimental surfaces

Here we study briefly the relationship between the selected images and how much reworked area they cover in the experiment. The original data set represented a time frame that equaled twice the amount of time required for flow to visit each pixel at least once (Figure 14 a,b). When the fraction of the experimental surface visited by flow in only the selected TIs are considered, it is encouraging to note that about 99.9% of the area visited by flow in the 136 time steps, has been visited by flow in just the small number of configurations in the chosen TIs (Figure 14, a-d). We also note that the selected images visit about 99% of the surface area

visited by all the flow patterns in the data-sets. In other words, by this heavily averaged metric the reworking "work" done by flow during the whole 136 minutes is similar to that done by the few representative images from each method, and 'representativeness' in geostatistical terms aligns with a simple physical metric that representative configurations should encompass near-complete visitation of the delta surface by water.

5 Generating a prior uncertainty model with direct sampling

Previously, we provided a broad overview of multiple-point geostatistics and what it aims to achieve; here, we present the results of generating geostatistical realizations based on the selected training images. Before doing so, we provide a brief overview of the specific algorithm used, namely direct sampling [*Mariethoz et al*., 2010]. Direct sampling (DS) is a sequential simulation method, meaning that it visits and simulates the grid-cells in the domain in random order. At every grid cell location, it extracts the configuration and values of already simulated grid-cells and finds in the training image a location with similar values in the neighborhood. This requires the definition of a distance (typically Euclidean) between the data in the simulation grid and the training image. Since an exact match cannot necessarily be found, a threshold t is used, such that the first matching event, by random search is below this threshold. The central location of that matching event is then pasted into the simulation domain. To aid the reproduction of complex, often non-stationary patterns (patterns that vary drastically over the domain), such as for the overhead snapshots, an auxiliary variable [*Chugunova and Hu*, 2008,] is used to guide the simulation. Such auxiliary variables are used to enforce trends (e.g. thin channel at the bottom, thick channel at the top). Figure 15 shows such auxiliary variables. In this particular case, we define two auxiliary variables. The first auxiliary variable accounts for the orientation of the deposits, which differs for each side of the tank. The second auxiliary variable accounts for the distance to the source of the injection of water & sediment and accounts for consistent downstream changes in the delta.

Figure 2 shows that the generated realizations are of the same theme as the training image, which is the very purpose of algorithms such as DS. We now need to generate a set of realizations per training image. Not each training image carries the same "weight" in the prior model, because the distribution of experimental delta images is not uniform. This is clearly the case when analyzing Figure 8, where some clusters contain a larger number of images. Hence, with a selection based on clustering, a natural way to decide on the number of realizations per training image is to retain the number of flume experiment images in the cluster containing the TI, as clustering groups images of similar variability.

In terms of selection based on the rate of change of the system, the number of realizations is defined by the number of snapshots between two peaks (Figure 10). For example, for large time intervals (e.g. 8-35 minutes), more realizations should be generated as images have similar properties compared to images that are close temporally. Conversely, for smaller time intervals (62-76 minutes), the system changes rapidly, hence fewer realizations of that pattern should be created.

For both sets of training images, we generated a total of 136 realizations using DS.

6 Comparing natural variability with MPS prior uncertainty

6.1 Comparison

We now return to the original question of whether or not the prior uncertainty created using MPS effectively mimics natural variability, for this well-controlled experimental case. To address this, we calculate the MHD between the generated MPS realizations of each of the two sets. Then we present a histogram and QQ-plot of these distances versus the distances of the binary images in the experiments, (Figure 16). We find similar variability in both distributions, with MPS realizations displaying slightly more middle-range distances.

This example shows that, MPS can reproduce the variability of the data-set as measured by MHD, given a proper selection of training images. If the training images are not properly chosen, there is no guarantee that MPS will reproduce the variability seen in the experiment. We discuss this point further in section 6.2.

It is also worth noting that despite the fact that MPS can reproduce the overall variability of the data-set, the realizations generated from a single TI do not reproduce the variability of the images in the same cluster for MHD, or between peaks for the rate of change. In other words, using a single TI, we underestimate the uncertainty for that particular TI, if that TI is regarded as representative of "a pattern" and the realizations considered equally likely to be drawn. This result also shows that the variance between the TIs is larger than the within TI variance, since otherwise we would not obtain an overall match to the variability (Figure 17). This issue has been discovered from probability theory itself in *Emery & Lantuejoul* [2014]. These authors found that the limited size of the training image, limits the pattern set and hence the “ergodic” variability of realizations generated from a single TI. It is clear that this issue is here mitigated by selecting multiple TIs.

6.2 Sensitivities

The choice of which training images and how many of them to use in MPS has a considerable impact on the MPS realizations variability. For example, a random selection of six training images, as illustrated in Figure 18, results in a prior model with too small uncertainty, as indicated by the deviation for the 45-degree line in the QQ-plot.

In addition, Figure 19 shows how the variability in the MPS realizations changes when the number of selected training images increases (selection using clustering with MHD). We can see that when a small number of TIs is used, the variability in the MPS realizations deviates from the 45 degree line in the QQ-plot, indicating a poor reproduction of variability. Starting at 5 TIs (the optimal number of clusters determined by the silhouette index), the variability becomes more similar. Note that a slight improvement for small distances is observed when larger number of TIs are selected, which can be explained by the fact that the “within” variability of each cluster is decreased.

Finally, a similar study was performed to evaluate the sensitivity of the MPS variability when the threshold *t* in DS is varied. The QQ-plots obtained for varying *t* are shown in Figure 20. For small values of *t*, the QQ-plot shows large overestimation of small distance, which can be explained by the fact that the MPS realizations will all be very similar to the TI, due to the small threshold. On the other hand, a large threshold would allow more deviation from the patterns found in the TIs (the MPS realization will be very different from the TI), hence more variability between the realizations.

All sensitivity analysis were done for both selection methods and provided similar results. For the sake of brevity, we only show results for the selection based on MHD and clustering,

7 Discussion

A fundamental problem in applying Bayesian information theory to physical systems is that of prior uncertainty. To specify the prior for sedimentary systems, one has to determine all the possible configurations of architectures that are deemed physically realistic and at what frequency (probability density) they occur. In this paper, we do not solve this problem, but rather start to understand the nature of the question and how to study this question with an eye on eventually developing practical methods. From a physical standpoint, we might say that the prior should represent our best understanding of what the most common or representative states of the physical system are. In a delta, for example, although there are indeed an infinity of potential channel configurations, these are not simply random networks; although complex, they are structured by the deterministic interplay of sediment and flowing water, mediated by biota and a host of other potential complicating factors. What constraints do the laws of morphodynamic evolution place on our Bayesian prior?

We focus here on a specific geostatistical method, where prior uncertainty is represented by a possibly infinite set of realizations. The method of MPS relies on specifying training images that contain patterns representative of the system and also associate prior frequencies to such training images, such as was done through clustering or the demon algorithm.

Here we propose to combine both geostatistical and process-oriented approaches to present a new perspective on the construction of a prior for a given sedimentary system. We use data from a physical experiment, involving steady deposition from a small-scale delta created under steady forcing. The system is already highly simplified relative to natural systems: it is free of vegetation and human influences, is supplied with only two kinds of (non-cohesive) sediment, and is not subject to discharge fluctuations, storms, tides, variable accommodation, or other external events. Thus the high resolution data from the physical experiment offer the opportunity to study natural variability within sedimentary systems in the absence of these other effects. Such data-sets enable us to test the quality of the prior by providing a basis against which to compare the variability of the resulting realizations. Moreover, it allows for a physical analysis of the prior model, which will help in understanding what particular patterns should appear in the definition of the prior for more complex natural cases.

Our prior model for MPS comprises a set of training images which we take as a small set of representative snapshots of the experiment, here discretized into wet/dry categories. We develop two distinct approaches for the selection of these images. The first approach uses distance-based model selection to ensure that only dissimilar images are chosen, irrespective of the temporal order of the images. The distance between two snapshots is defined by the

MHD, which measures geometric differences in images. The second approach analyzes the displacement of deposits as an explicit function of time and selects models based on a local measure of the rate of change. In both cases, the prior comprises only a few images (5 and 6 respectively). Even though the selected images are not the same (which is expected), they are relatively close in time and exhibit similar geometries. Although alternative criteria for the selection of a set of representative images could be used as well, we find this similarity between the two independent approaches very encouraging.

Our investigations demonstrate that by carefully selecting a set of training images, MPS can reproduce fairly accurately the variability of the delta deposit under study for the given variability measure. The variability of a set of image is defined using dissimilarity measures (MHD) estimated between any two pairs of images. Analysis of the MHD distribution between the two sets of images (MPS realizations and photographs) is a good comparison of the uncertainty space covered by both sets of images. Alternative measures of variability may lead to different results and should be investigated, but we believe that the approaches we have presented here represent a viable way of selecting the representative 'eigen pattern' images, and that the number of images (5-6) is a good estimate of the size of a minimum set needed to capture uncertainty in pattern modeling for this case.

This study addresses only the question of the definition of the training images and assumes fixed auxiliary variables. Evidently, auxiliary variables are part of the prior model, and could be varied as well. This would be of crucial importance when the set of selected training images are transformation invariant (e.g. rotation, translation, etc.), hence a more specific auxiliary variable, related to some characteristics of the TIs could be generated to increase variability in the MPS realizations.

In order to compare geostatistical variability with the known variability of the experiment, we used important dynamic information of the experimental delta. This allowed us not only to select TIs, but also to determine the prior probability associated with each TI, which is taken as proportional to the frequency of the pattern in the experiment. This latter information is also essential in modeling variability. However, in the absence of some or all this information, the question of how to generate a good prior with purely static information (e.g.: from a set of seismic attribute maps) remains to be investigated.

We suggest that some clues to the selection of appropriate training images lie in the physical properties of the two sets of selected images from this experiment. Three obvious attributes of both sets are that they include 1) each of the three basic surface configurations, i.e. channelized flow, sheet flow and an intermediate, as well as 2) trivial geometric transformations of each, in such a way that 3) 99% of the surface area of our sedimentary system was visited by flow at least once. We consider it very encouraging that the eigen-patterns, identified geometrically without reference to process dynamics, nonetheless correspond to fundamental dynamic modes of the system identified in previous studies (channelization/incision, sheet flow/deposition). Additional MPS investigations of experiments with different but steady boundary conditions may offer insight into how much the construction of the prior model depends on the dynamics of the system under consideration. Refining metrics such as the reworking time-scale or the ratio of overbank to channel deposits may improve the linkage between stratigraphy and system dynamics.

In this paper, we have limited ourselves to studying autogenetic cycles. Because such cycles repeat themselves, it appears that a finite amount of training images can describe well the observed natural variability. A this point, it is unclear whether this is the case for non-autogenic data, how the techniques should be adapted and how training images should be selected, whether a finite set of TIs is able to capture such variability. This is still work in progress

8 Conclusions

Applying advanced multi-point geostatistics to a set of experimental delta images that represent the autogenic (intrinsic) pattern variability of a controlled, simplified depositional system, we find that:

1. Using a combination of distance metrics and clustering algorithms, a set of 136 surface patterns can be distilled down to 5-6 ‘eigen-pattern’ training images that represent the fundamental patterns in the set.

2. The eigen-pattern sets can be identified using either image-image distance irrespective of position in the time sequence (5 images), or using a temporal-change metric in which the eigen-pattern images represent periods of relative temporal pattern stability (6 images). Encouragingly, the sizes and general characteristics of the eigen-pattern image sets identified in these two complementary ways are similar.

3. Applying direct sampling to these ‘eigen-pattern’ sets of training images allows simulation of the original full pattern set with reasonable fidelity, although the uncertainty in the full set is still somewhat underestimated.

4. The eigen-pattern training image sets display patterns consistent with previous physical interpretations of the fundamental modes of this type of delta system: a highly channelized, incisional mode; a poorly channelized, depositional mode; and an intermediate mode.

Acknowledgements

The data used in this study was collected during an experiment carried out in the Tulane Delta Basin in 2010 and first used in Wang et al., 2011. The overhead photographs used in this study is a sub-set of the data stored at:
https://sen.ncsa.illinois.edu/acr/#collection?uri=tag:cet.ncsa.uiuc.edu,2008:/bean/Collection/56273960-D470-496A-9552-667832CC2997

References

Bayes, T, and Price, R, 1763, An Essay towards solving a Problem in the Doctrine of Chance. By the late Rev. Mr. Bayes, communicated by Mr. Price, in a letter to John Canton, A. M. F. R. S.. Philosophical Transactions of the Royal Society of London 53 (0): 370–418.

Borg I., Groenen P., 1997, Modern multidimensional scaling: theory and applications. Springer, New York, 614 p.

Caers, J., 2011, Modeling Uncertainty in the Earth Sciences, Wiley Blackwell.

Caers, J., and T. Zhang, 2004, Multiple-point geostatistics: a quantitative vehicle for integrating geologic analogs into multiple reservoir models, in Integration of outcrop and modern analog data in reservoir models, AAPG memoir 80, edited by G. M. Grammer, Harris, P. M., and Eberli, G. P., pp. 383-394, American Association of Petroleum Geologists, Tulsa.

Chugunova, T. and Hu, L.Y., 2008, Multiple-Point Simulations Constrained by Continuous Auxiliary Data. Mathematical Geosciences. 40(2), 133–146.

Cover, T.M. and Thomas, J.A., 2012. Elements of information theory. John Wiley & Sons.

Dempster, A. P., 1967, Upper and lower probabilities induced by a multivalued mapping. The Annals of Mathematical Statistics 38 (2): 325–339.

Demyanov, V., Backhouse, L. and Christie, M., 2015. Geological feature selection in reservoir modelling and history matching with Multiple Kernel Learning. Computers & Geosciences, 85, pp.16-25.

Dubuisson, M-P., and Jain, A.K., 1994, A modified Hausdorff distance for object matching. In: Proceedings of the 12th International Conference on Pattern Recognition, A, 566-568.

Emery, X. and Lantuéjoul, C., 2014. Can a training image be a substitute for a random field model?. Mathematical Geosciences, 46(2), pp.133-147.

Feyen, L. and Caers, J., 2006. Quantifying geological uncertainty for flow and transport modeling in multi-modal heterogeneous formations. Advances in Water Resources, 29(6), pp.912-929.

Gómez-Hernández, J.J. and Wen, X.H., 1998. To be or not to be multi-Gaussian? A reflection on stochastic hydrogeology. Advances in Water Resources, 21(1), pp.47-61.

Jaynes, E.T., 2003. Probability theory: the logic of science. Cambridge university press.

Kindermann, R., Snell, J. Laurie, (1980). Markov Random Fields and their Applications. Rhode Island: American Mathematical Society.

Kim, W., A. L. Petter, K. Straub, and D. Mohrig (2014), Investigating the autogenic process response to allogenic forcing: Experimental geomorphology and stratigraphy, in From Depositional Systems to Sedimentary Successions on the Norwegian Continental Margin, edited by A. W. Martinius, R. Ravnas, J. A. Howell, R. J. Steel and J. P. Wonham, pp. 127-138, IAS Special Publication.

Lanzoni, S., and Seminara, G., 2006, On the nature of meander instability. Journal of Geophysical Research.F.Earth
Surface, 111doi:http://dx.doi.org/10.1029/2005JF000416.

Li, L., Caers, J. and Sava, P.: Assessing seismic uncertainty via geostatistical velocity-model perturbation and image registration: An application to subsalt imaging. The Leading Edge, 34(9), 1064–1066. (2015).

Liang, M., Van Dyk, C. and Passalacqua, P., 2016. Quantifying the patterns and dynamics of river deltas under conditions of steady forcing and relative sea level rise. Journal of Geophysical Research: Earth Surface.

Linde, N., Renard, P., Mukerji, T. and Caers, J., 2015. Geological realism in hydrogeological and geophysical inverse modeling: A review. Advances in Water Resources, 86, pp.86-101.

Mariethoz G., Renard P., Straubhaar J., 2010, the direct sampling method to perform multiplepoints simulations. Water Resources Research VOL. 46, W11536.

Mariethoz G. and Caers J., 2015 Multiple-Point Geostatistics: stochastic modeling with training images, Wiley Blackwell.

Otsu, N., 1975. A threshold selection method from gray-level histograms. Automatica, 11(285-296), pp.23-27.

Park H., Scheidt C., Fenwick D., Boucher A. and Caers J., 2013. History matching and uncertainty quantification of facies models with multiple geological interpretations. Computational Geosciences. 17 (4):609-621.

Rousseeuw, P.J., 1987. Silhouettes: a graphical aid to the interpretation and validation of cluster analysis. Journal of Computational and Applied Mathematics. 20, 53–65.

Shafer, G., 1976, A Mathematical Theory of Evidence, Princeton University Press.

Shannon, C.E., 1949, A Mathematical Theory of Communication. Bell System Technical Journal 27 (3): 379–423.

Scheidt, C., Caers, J., 2009a Representing spatial uncertainty using distances and kernels. Mathematical Geosciences. 41(4), 397–419.

Scheidt C. and Caers J., 2009b Uncertainty Quantification in Reservoir Performance Using Distances and Kernel Methods – Application to a West-Africa Deepwater Turbidite Reservoir. SPE J, 14 (4):680:692, SPEJ 118740-PA.

Scheidt, C., Tahmasebi, P., Pontiggia, M., Da Pra, A. and Caers, J., 2015. Updating joint uncertainty in trend and depositional scenario for reservoir exploration and early appraisal. Computational Geosciences, 19(4), pp.805-820.

Serfling, R., 2002. Quantile functions for multivariate analysis: approaches and applications. Statistica Neerlandica, 56(2), pp.214-232.

Sheets, B., Hickson, T.A., and Paola, C., 2002. Assembling the stratigraphic record: Depositional patterns and time-scales in an experimental alluvial basin: Basin Research, v. 14, p. 287.

Strebelle, S., 2002. Conditional simulation of complex geological structures using multiple-point statistics. Mathematical Geology, 34(1), pp.1-21.

Suzuki, S. and Caers, J., 2008, A Distance-Based Prior Model Parameterization for Constraining Solutions of Spatial Inverse Problems. Mathematical Geosciences, 40, 4, 445-469.

Suzuki, S., Caumon, G. and Caers, J., 2008, Dynamic Data Integration Into Structural Modeling: Model Screening Approach Using a Distance-based Model Parameterization, Computational Geosciences, 12, 1, 105-119.

Tan, X., Tahmasebi, P. and Caers, J., 2014. Comparing training-image based algorithms using an analysis of distance. Mathematical Geosciences, 46(2), pp.149-169.

Thirion J.P., 1996, Non-rigid matching using demons Proc. CVPR '96, 1996 IEEE Computer Society Conf. Computer Vision and Pattern Recognition pp 245–51.

Vorosmarty, C. J., Ericson, J. P., Dingman, S. L., Ward, L. G., & Meybeck, M. (2007). Future impacts of freshwater resource management; sensitivity of coastal deltas. IAHS-AISH Publication, 314, 231-238.

Wang, Y., Straub, K. M., and Hajek, E. L., 2011, Scale-dependent compensational stacking: An estimate of autogenic time scales in channelized sedimentary deposits, Geology; v. 39; no. 9; p. 811–814; doi:10.1130/G32068.

Wickert, A. D., J. M. Martin, M. Tal, W. Kim, B. Sheets, and C. Paola, 2013, River channel lateral mobility: metrics, time scales, and controls, J. Geophys. Res. Earth Surf., 118, 396–412, doi:10.1029/2012JF002386.

Zadeh, L., 1978, Fuzzy Sets as the Basis for a Theory of Possibility, Fuzzy Sets and Systems 1:3–28.

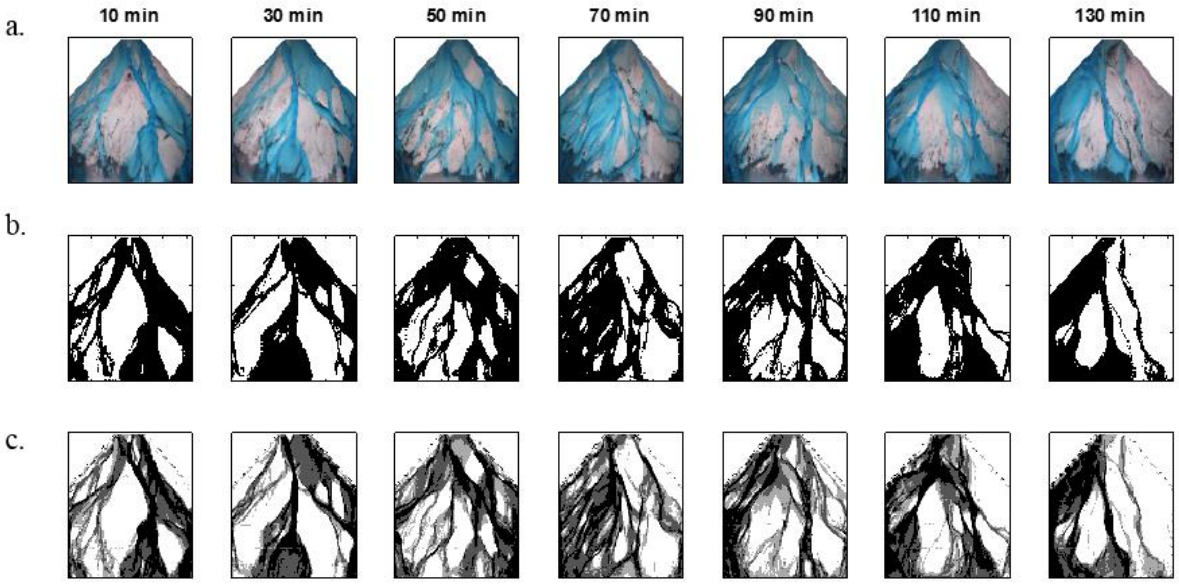

Figure 1. Examples of a few images of the flume experiment for different time. Flow in these photographs is from top to bottom. (a) Snapshots of the experiments. The blue pixels indicate locations where flow (containing blue food dye) moves over the surface. The black sediment is coal which is the most mobile fraction of the sediment mixture, and the tan sediment is sand (b) Binary representation of the snapshots. Black represents wet (flow) pixels, white represent dry (no flow) pixels. (c) Categorized snapshots. The thresholding was achieved using Otsu's method [*Otsu*, 1975]. White represent dry pixels, gray represent wet pixels. The lighter the gray, the shallower the flow is.

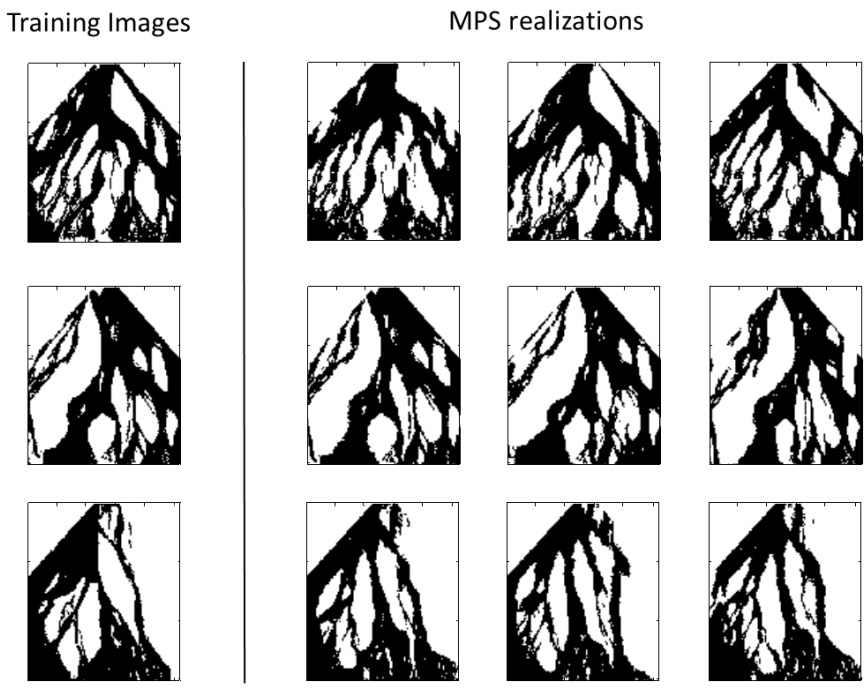

Figure 2. MPS simulation: (left) example of training images, (right) example of MPS realizations. Note that the MPS realizations realistically reproduce the patterns found in the training image.

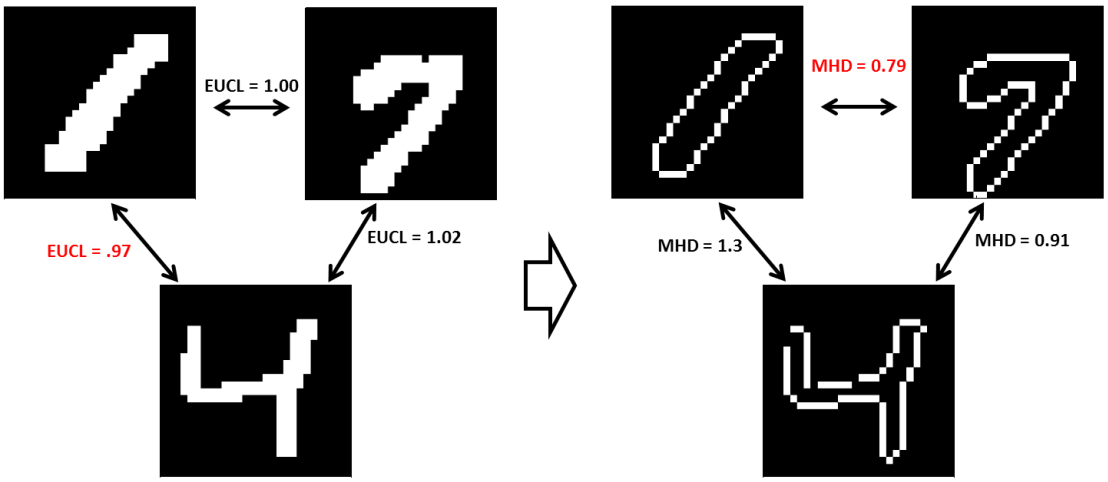

Figure 3. Evaluation of the modified Hausdorff distance for images of numbers 1, 4 and 7. MHD requires the regularization of the images into points sets (shown in right). The smallest MHD is observed between images of 1 and 7, which is consistent with visual inspection. This is not the case for the pixel by pixel Euclidean distance (left).

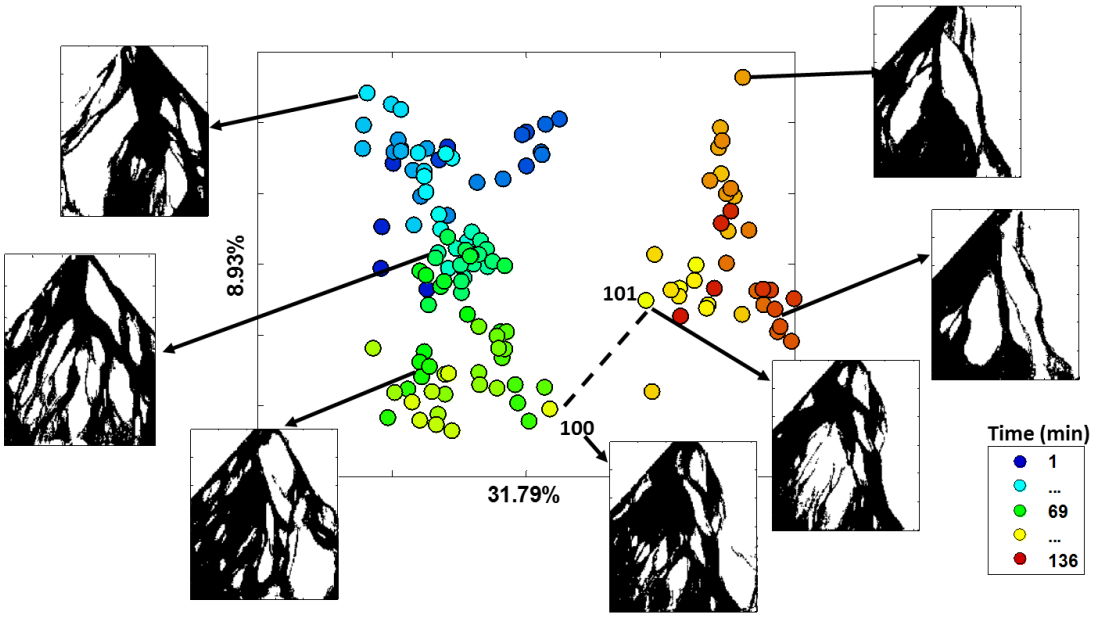

Figure 4. 2D MDS plot based on the MHD between pairs of images. Each point on the plot represents an image. The scale on the axis is not shown because it is not relevant; what is relevant is the shape of the scatterplot and the relative (Euclidean) distance between the points/images. The percentages on the axis are the percentage of variance each dimension provides towards representing the MHD.

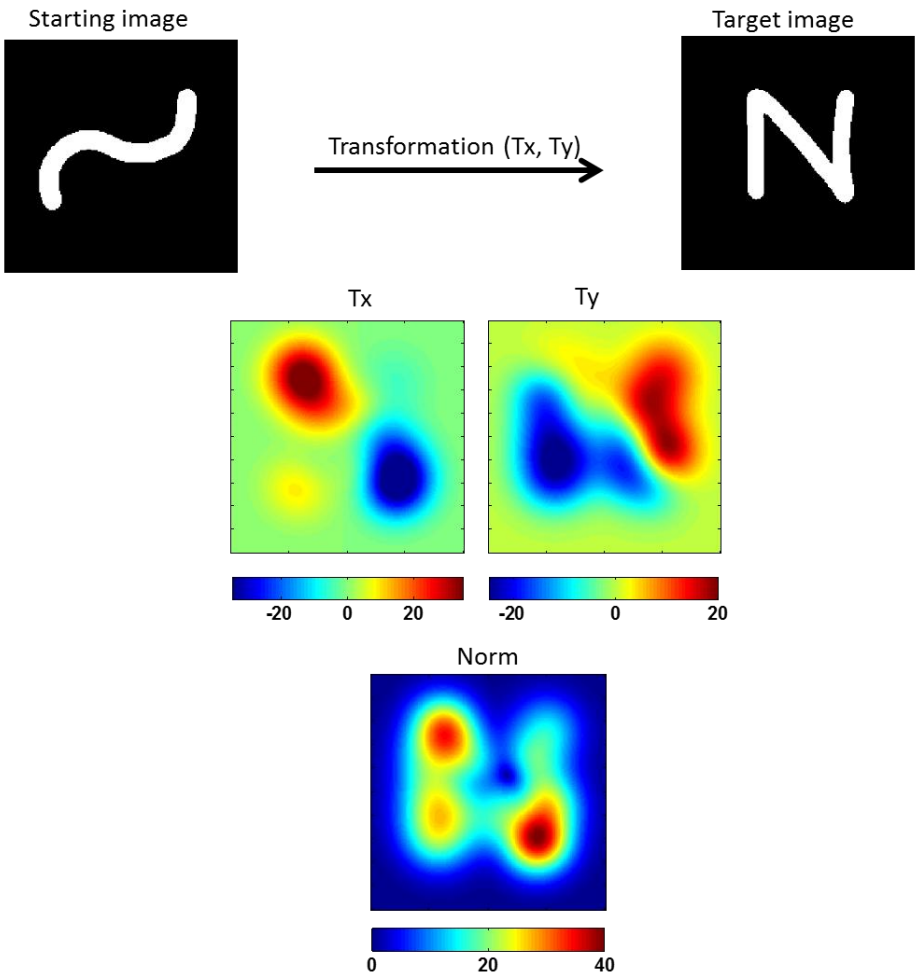

Figure 5. Illustration of the demon algorithm. Demon evaluates the transformation (in number of pixels) Tx and Ty to apply on the starting image to get an image similar to the target image. The resulting norm (total deformation in terms of an x and y component) indicates areas of large change (red) and little change (blue).

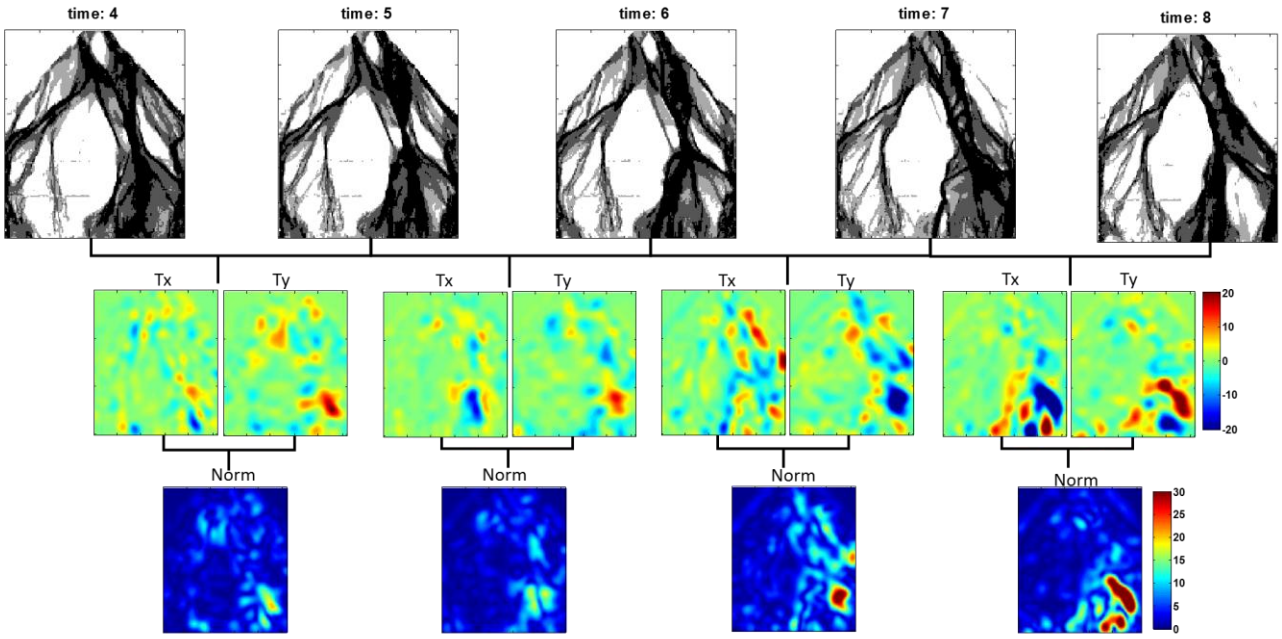

Figure 6. Example of channel migration using the demon algorithm. The norm indicates the location of the large changes in the system. Here, reorganization in the channel network is seen between time 7 and 8, in the lower right corner.

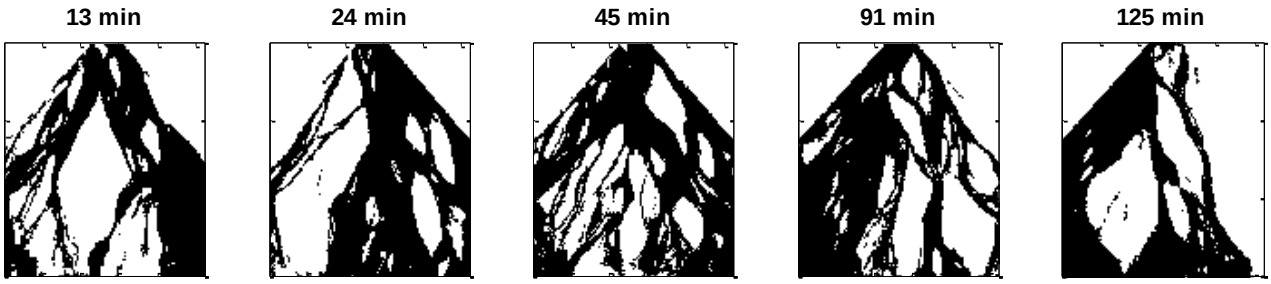

Figure 7. Selected images by clustering based on the MHD. The value at the top of the image represents the time in minutes of the experiment.

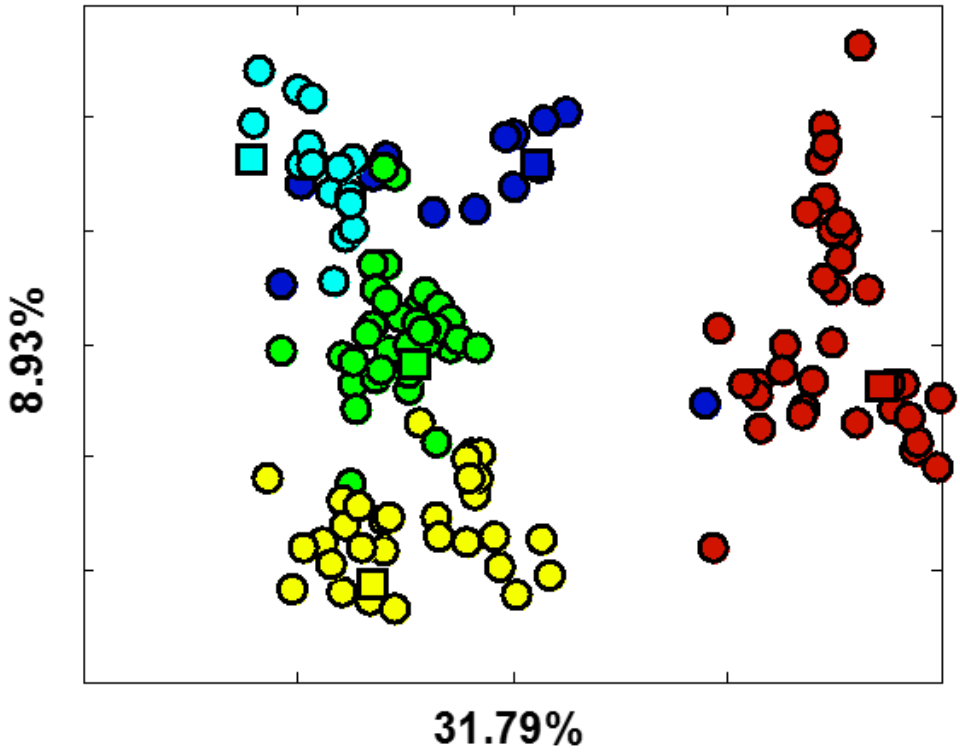

Figure 8. MDS plot with five clusters and five centroids (squares)

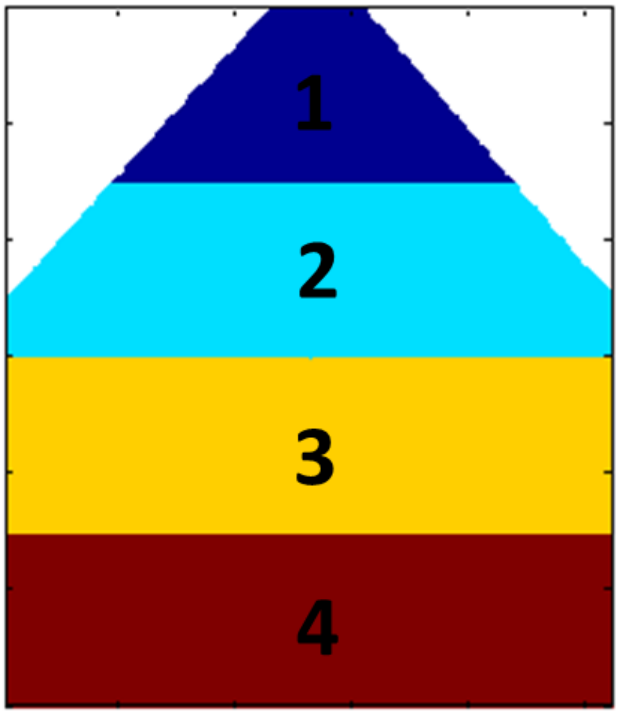

Figure 9. Four regions used to estimate a local rate of change. Regions are created based upon their proximity to the source of sediments.

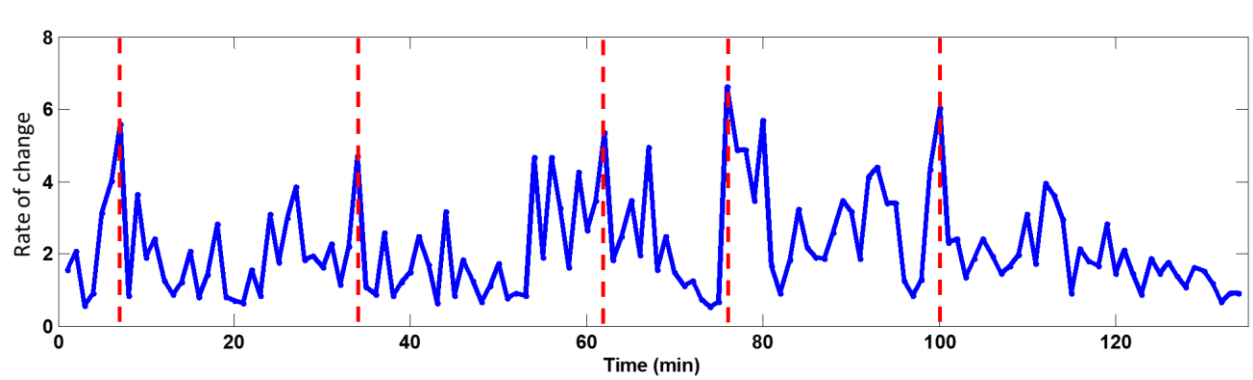

Figure 10. Rate of change between consecutive images of the experimental delta. The peaks (red dotted lines) show the highest changes (the differences in the change between two consecutive images is important).

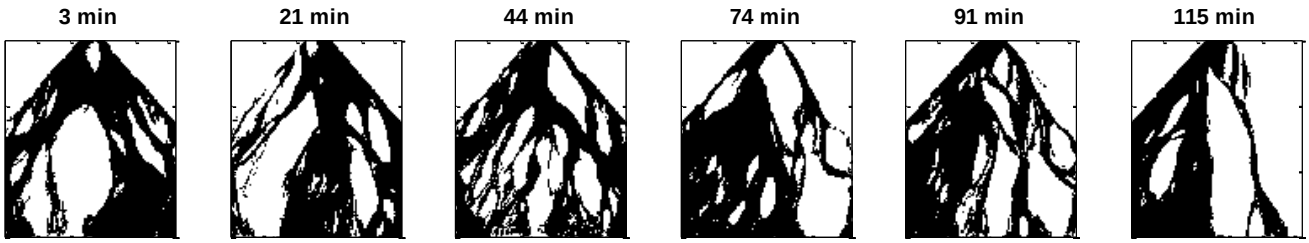

Figure 11. Selected images based in the rate of change. The value at the top of the image represents the time in minutes of the experiment.

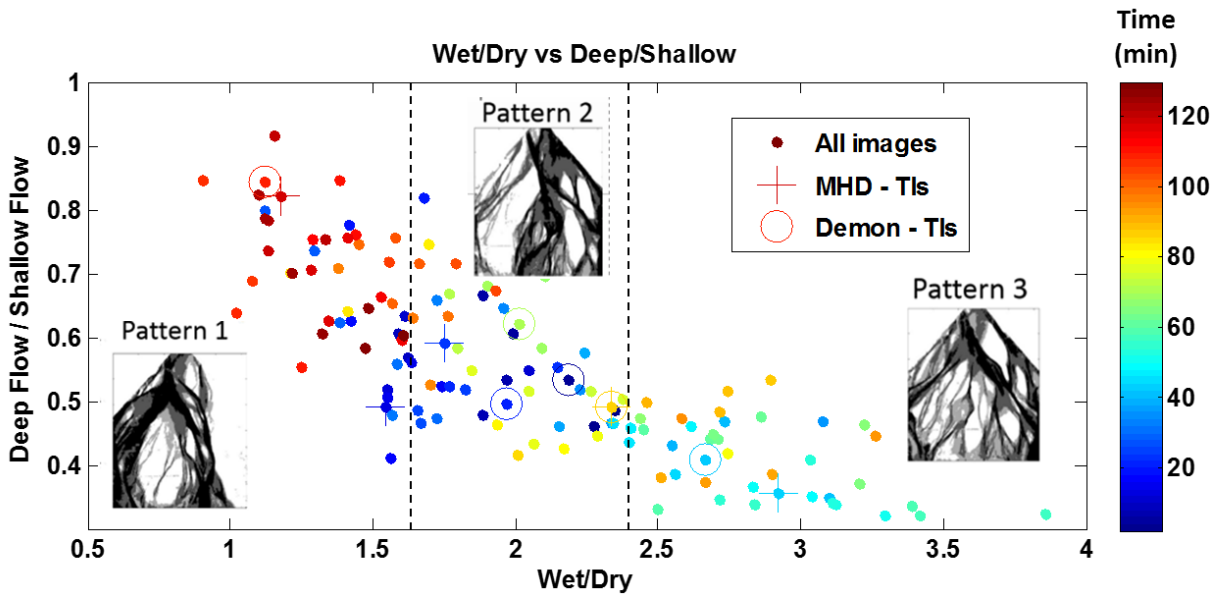

Figure 12. The ratio of "wet" to "dry" pixels plotted against the ratio of "deep" to "shallow" flow defines the continuum from incision to deposition. Small dots represent each image used in the data-set, the circles and crosses represent the training images selected through the MHD and demon protocols respectively. The selected training images in both methods encompass the whole range of configurations

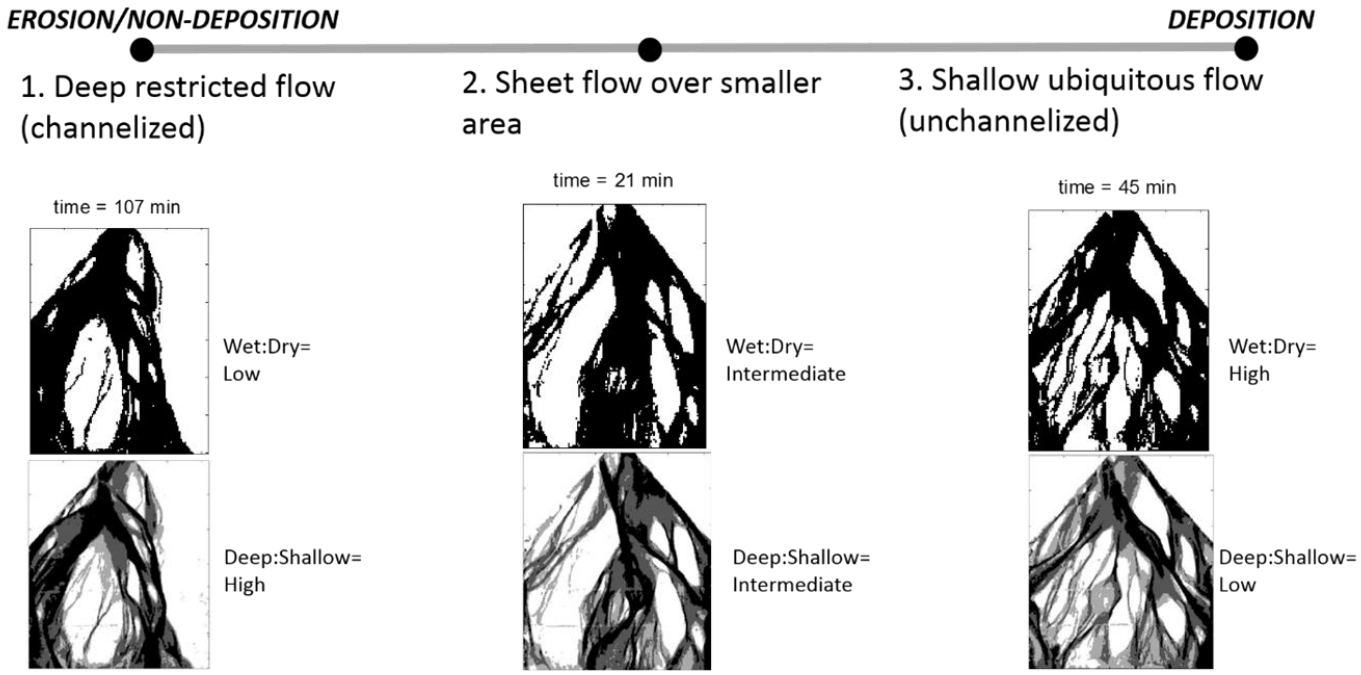

Figure 13. Training images are divided into those typified by sheet flow, by channelized flow and by an intermediate between the two end members. Channelized flow is characterized by a low ratio of wet to dry pixels and a high ratio of deep to shallow flow; sheet flow cases display a high ratio of wet to dry pixels and a low ratio of deep to shallow flow; the intermediate case falls in the continuum between sheet flow and channelized flow.

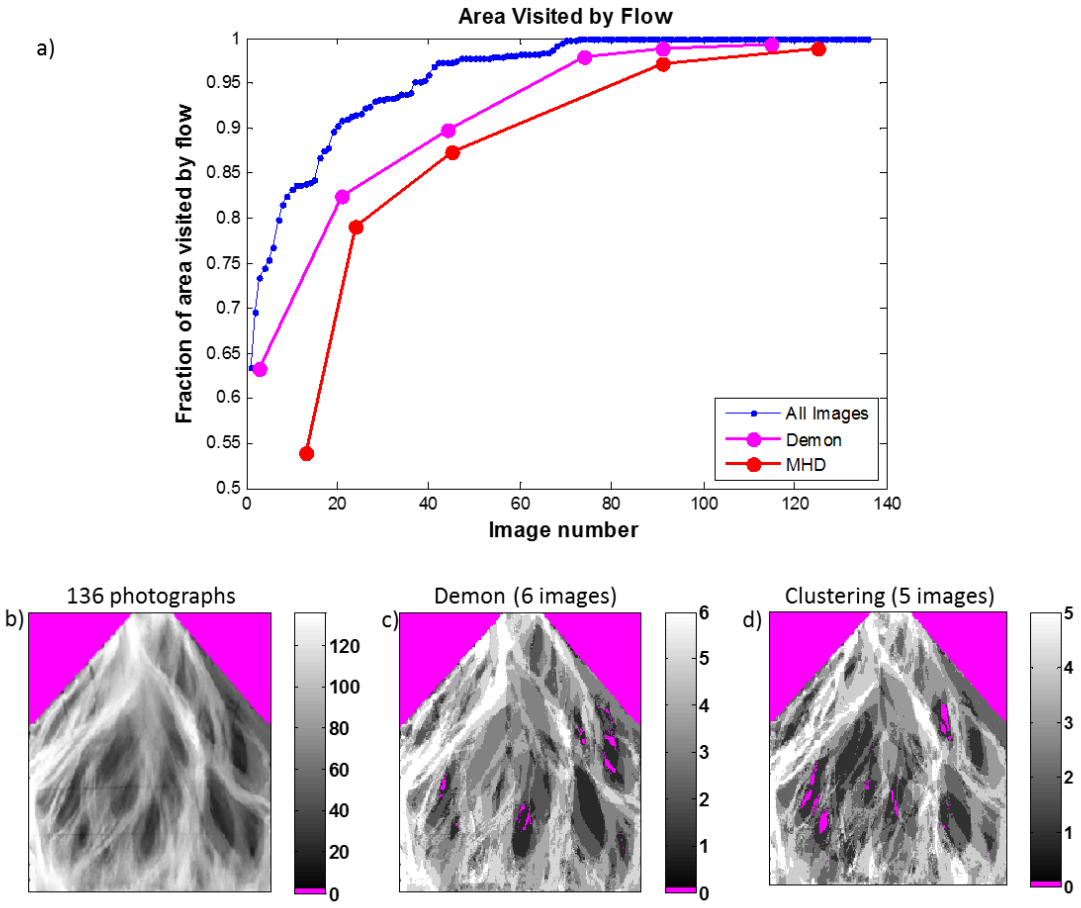

Figure 14. (a) The cumulative flow visitation curve gives the fraction of the surface area of the experiment that has been visited by flow through time. The small dots represent the cumulative fraction of the area visited through each time step in the 136 images. Note that 68 time steps (minutes) were required for flow to visit every pixel and that our data-set comprises twice that number of consecutive images. The small number of TIs (large dots) cover about 99% of the surface area visited by flow. b, c, d are flow occupation maps created by summing up the binary matrices of the images in (b) the whole data-set of 136 images, (c) the demon TI set, and (d) the MHD TI set. Magenta shading represents the small area not visited by flow in any of the training images

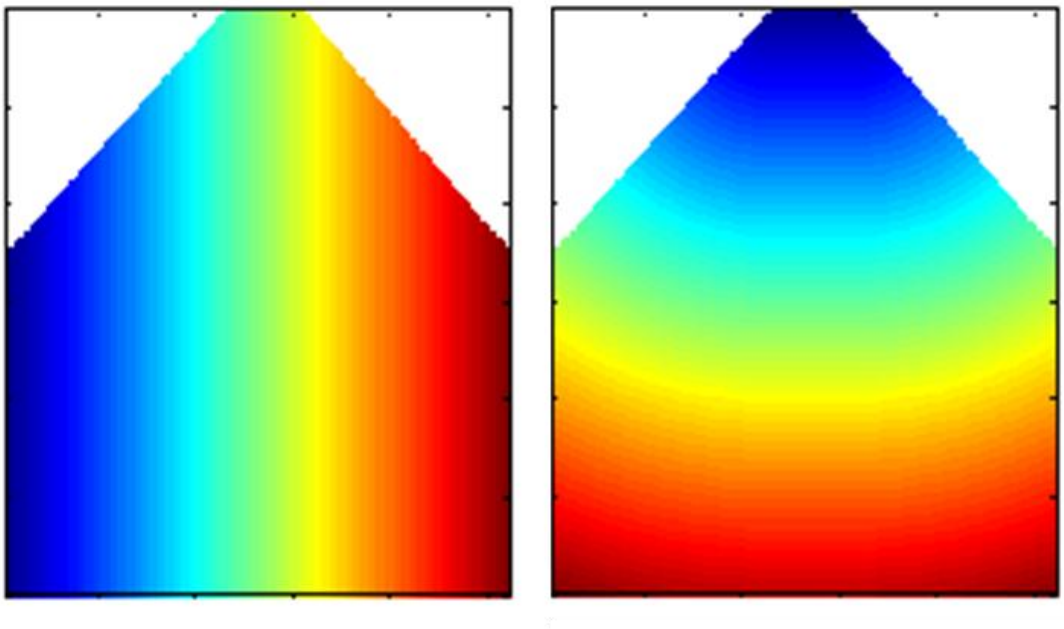

Figure 15. Two auxiliary variables are used in direct sampling to account for the orientation of the deposits (left) and distance to the source of sediment injection (right)

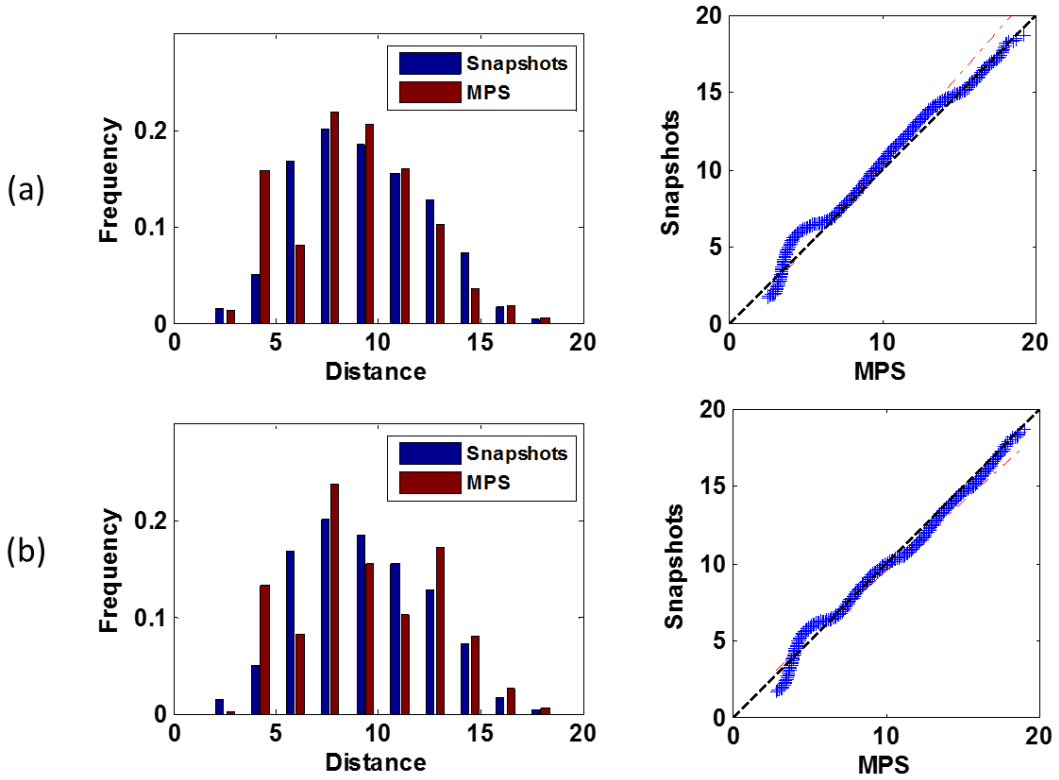

Figure 16. (a) Histograms and QQ-plot of the MHD distances between the 136 images from the experiment and 136 images generated using DS. The training images are the five images selected with the MHD distance (b) similar, but with the 6 training images selected via the demon algorithm

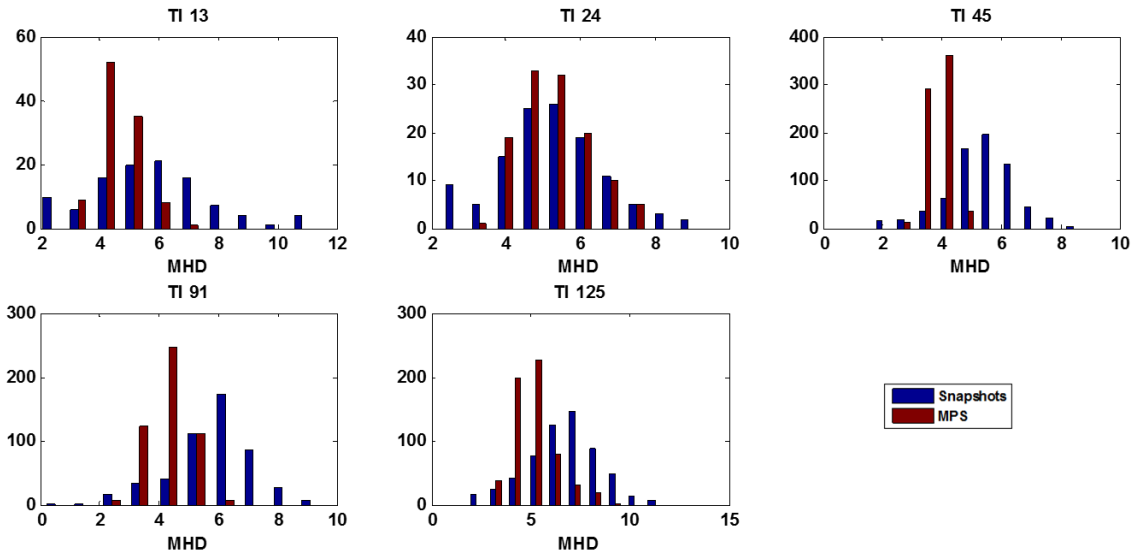

Figure 17. Comparison of the variability, as defined by MHD, between generated realizations per each training image and the flume experiment images closest (in MHD) to the selected TI.

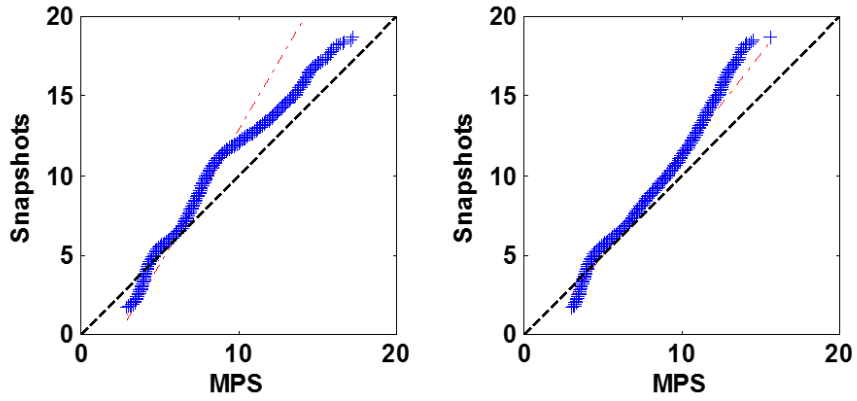

Figure 18. Comparison of the variability, as defined by MHD, of the set of 136 original images and the MPS realizations based on 6 randomly selected training images. Example for two different random selections. The variability is not as well reproduced (underestimated) for the random selection.

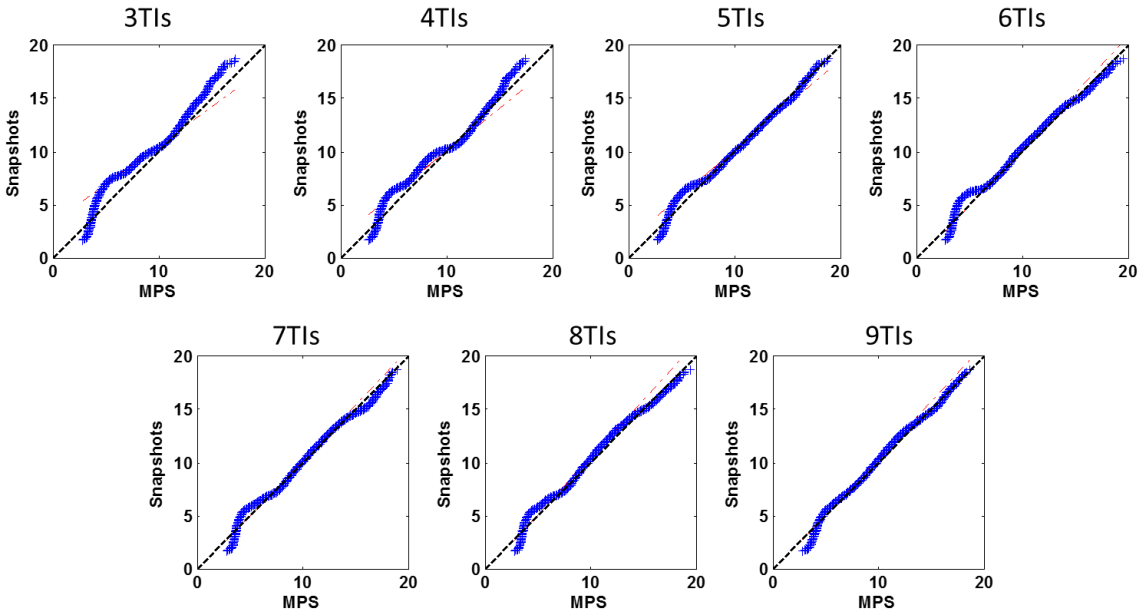

Figure 19. QQ-plot comparing variability in the original images with variability in the MPS realizations when 3 to 9 TIs are selected using k-medoid on MHD. The study presented above used 5 TIs, as suggested by the silhouette index.

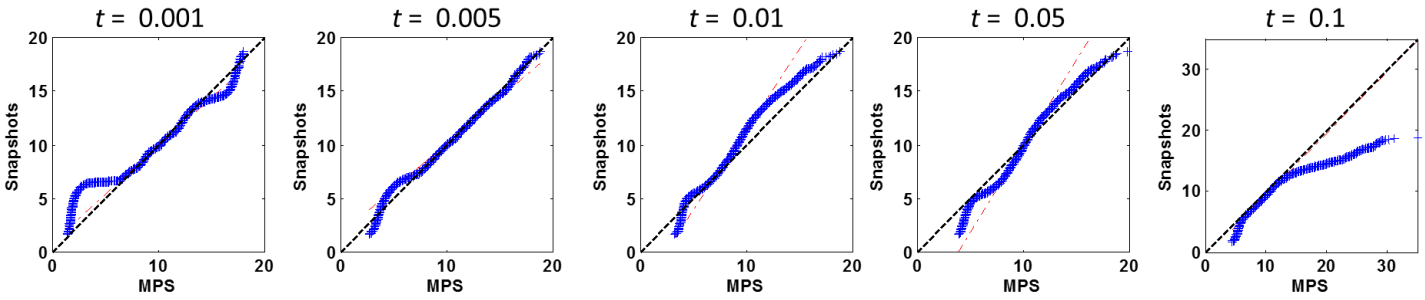

Figure 20. QQ-plot comparing variability in the original with variability in the MPS realizations when the threshold *t* in DS is varied, using the 5 TIs selected by clustering. Previous results where shown for $t = 0.005$.